Counterion distribution near a monolayer of variable charge density

A Letters Journal Exploring the Frontiers of Physics

July 2007

EPL, **79** (2007) 18003
doi: 10.1209/0295-5075/79/18003

www.epljournal.org

Counterion distribution near a monolayer of variable charge density

K. Giewekemeyer and T. Salditt

Institut für Röntgenphysik - Friedrich-Hund Platz 1, 37077 Göttingen, Germany

received 14 February 2007; accepted in final form 21 May 2007
published online 19 June 2007

PACS 87.16.Dg – Membranes, bilayers, and vesicles
PACS 83.85.Hf – X-ray and neutron scattering
PACS 68.08.-p – Liquid-solid interfaces

Abstract – We study the bromide counterion distribution near a solid-supported monolayer in the case of vanishing bulk electrolyte concentration by resonant X-ray reflectivity. The surface charge density of the monolayer was varied by using different molar ratios of the cationic Di-Octadecyl-Di-methyl-Ammonium-Bromide (DODAB) and the neutral Di-Palmitoyl-Glycero-Phosphocholine (DPPC). The analysis, either based on a conventional box model with an additional counterion contribution, or based on an independent unbiased global optimization approach, yields a good agreement with the classical Poisson-Boltzmann theory for the salt-free case.

Introduction. – The distribution of counterions in the vicinity of charged macroions immersed in an aqueous solution has been predicted almost 100 years ago [1–3], and has become a cornerstone of colloidal and macromolecular science. The distribution and release of counterions determine self-assembly properties, phase behavior and interaction forces of macromolecules in solution. Recent theoretical work has addressed the problem beyond the classical Poisson-Boltzmann (PB) approach, including effects of quantum chemistry, polarity of water, discreteness of surface charges, counterion radius, and ion-ion correlation effects, see [4] for an overview. The central structural property is the counterion distribution in the solvent. Experimentally, the concentration at the interface has been studied in bulk electrolytes for different macroions, such as DNA [5,6], synthetic polyelectrolytes [7] or multilamellar vesicles [8,9]. Only recently, the counterion distribution itself has been studied at molecular resolution, taking advantage of aligned geometries such as charged Langmuir monolayers in contact with electrolyte solutions of varied concentration [10,11], the interface between two electrolyte solutions containing different charged compounds [12], or the mica-water interface [13]. Here we extend these efforts in addressing the case of a flat uniformly charged wall in salt-free solution with counterions only (cf. fig. 1), where the surface charge density σ_s is used as an external control parameter. This case is experimentally difficult, but important, since a considerable amount of recent theoretical work has been devoted to it [4,14–16]. In this letter we present an X-ray reflectivity study of the counterion distribution near a planar charged solid-supported monolayer in the salt-free case, including contrast variation at photon energies around the BrK_α absorption edge.

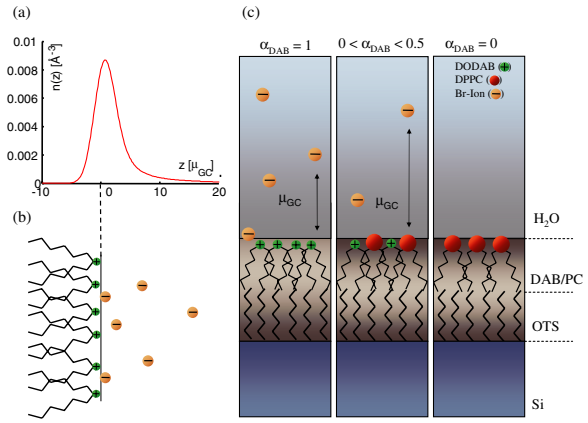

Fig. 1: (a) Counterion distribution $n(x)$ near a monolayer with surface charge density σ_s. The idealized Poisson-Boltzmann distribution is convoluted with a Gaussian of width ξ to account for experimental broadening of the profile. (b) Sketch of a DODAB monolayer with bromide counterions. (c) Sketch of the mixed monolayer on a silanized silicon wafer, for three different charged molar fractions α_{DAB}. The corresponding Gouy-Chapman length μ_{GC} increases with decreasing σ_s and becomes infinite for an uncharged surface.

The system depicted in fig. 1(b) is described by a 1-d Poisson-Boltzmann equation, given by $\mathrm{d}^2\bar{V}/\mathrm{d}z^2 = 4\pi\ell_B n_0 \exp[\bar{V}(z)]$, with the potential $\bar{V}$ rescaled in units of k_BT/e_0 and the z-coordinate in the direction normal to the charged interface. ℓ_B denotes the Bjerrum-length, which is about 7.1 Å in water at room temperature, and σ_s the surface ion number (or charge) density. Furthermore, n_0 denotes the counterion density at the interface ($z=0$). Applying the contact-value theorem $n_0 = 2\pi\ell_B\sigma_s^2$ for the present system [4], the PB equation yields the analytical result of a logarithmically decaying potential and a counterion distribution

$$n(\bar{z}) = \frac{\sigma_s}{\mu_{\mathrm{GC}}} \cdot \frac{1}{(\bar{z}+1)^2} = \frac{\sigma_s}{\mu_{\mathrm{GC}}} \cdot \frac{1}{\left(\frac{z}{\mu_{\mathrm{GC}}}+1\right)^2} \qquad (1)$$

with $\bar{z}$ rescaled in Gouy-Chapman-lengths $\mu_{\mathrm{GC}} = (2\pi\ell_B\sigma_s)^{-1}$. Thus, the central result here is the algebraic dependence of $n(\bar{z})$.

Materials and methods. – Experimentally, a flat charged wall of controlled charge density σ_s in salt-free ultra-pure water (Millipore) was realized by deposition of a solid-supported cationic monolayer with bromide counterions on top of a silanized silicon wafer, see fig. 1(c). First, Octadecyl-tri-chloro-silane (OTS, $C_{18}H_{37}SiCl_3$) was covalently bound to cleaned silicon wafers, following the standard procedures as described in [17]. Second, a monolayer composed of mixtures of the cationic double-chain surfactant Di-Octadecyl-Di-methyl-Ammonium-Bromide (DODAB) and the neutral co-lipid 1,2-Dipalmitoyl-sn-Glycero-3-Phosphocholine (DPPC), both obtained from Avanti Polar Lipids (Alabaster, AL, USA), at varied DODAB molar fractions $\alpha_{\mathrm{DAB}} = 1$, 0.5, 0.25, 0, was deposited using the well-known vesicle fusion method [18,19]. Note that DPPC has been used before as a "natural co-lipid" for charge dilution of DODAB [20]. To verify that the results did not depend on a particular preparation pathway, an alternative protocol based on thermal desorption of a thick multilamellar stack of charged DODAB bilayers was also investigated, leaving behind the charged monolayer [21] with essentially the same structural results, but sometimes inferior sample quality. For this study DODAB was chosen for reasons of contrast, as detailed in the following. The 36 electron bromide counterion with an an average electron density of $\rho_{\nu_{\mathrm{Br}}} = 1.357\,\text{Å}^{-3}$ at an ionic volume of $\nu_{\mathrm{Br}} = 26.5\,\text{Å}^3$ [12] is considerably higher than the DODAB-($NC_4H_{10}^+$)-headgroup electron density of $\rho_{\nu_{\mathrm{HG}}} = 0.401\,\text{Å}^{-3}$, calculated based on a Van-der-Waals volume of $\nu_{\mathrm{HG}} = 99.7\,\text{Å}^3$ (see footnote [1]). However, X-ray reflectivity is only sensitive to the electron density averaged over the ionic or Van-der-Waals volume, respectively, *and* the laterally surrounding space, which is filled up with water molecules. Considering a DODAB area per headgroup of $A_{\mathrm{HG}} = 55\,\text{Å}^2$ [22,23] one can estimate the total-densities in the laterally space-filling volume V_{HG} of the headgroup and V_{Br} of the bromide to be $\bar{\rho}_{\mathrm{HG}} = \rho_{\nu_{\mathrm{HG}}} \cdot \frac{\nu_{\mathrm{HG}}}{V_{\mathrm{HG}}} + \rho_{\mathrm{H_2O}} \cdot \frac{V_{\mathrm{HG}}-\nu_{\mathrm{HG}}}{V_{\mathrm{HG}}} = 0.367\,\mathrm{e}/\text{Å}^3$ and $\bar{\rho}_{\mathrm{Br}} = 0.467\,\text{Å}^3$, respectively. Consequently, the average DODAB headgroup density $\bar{\rho}_{\mathrm{HG}}$ is very close to the density of water ($\rho_{\mathrm{H_2O}} = 0.334\,\mathrm{e}/\text{Å}^3$), so that the density originating from the headgroup area is highly dominated by the bromide density $\bar{\rho}_{\mathrm{Br}}$.

In addition to the variation of the charged molar fraction α_{DAB}, contrast variation by resonant X-ray scattering was used for fixed α_{DAB}. More specifically, the effective number of scattering bromide electrons was changed selectively by varying the incident photon energy around the Br K_α edge.

The sample deposition was performed in a sealed and temperature-controlled teflon cell equipped with Kapton windows and a 10 mm water path for the X-ray reflectivity experiment. After flushing the sample cell with ultrapure water, it was mounted onto the z-axis diffractometer (Huber tower) of the ID01 undulator beamline of the European Synchrotron Radiation Facility (ESRF, Grenoble). The beam was monochromatized by a double crystal Si(311) monochromator with an energy resolution of 1 eV, calibrated by NaBr solutions for photon energies E around the Br K_α absorption edge. The dispersion correction f'_{Br} to the bromide atomic form factor $f^{(0)}_{\mathrm{Br}}$ needed for contrast variation was calculated from energy-dependent bromide fluorescence scans, exploiting Kramers-Kronig relations using the CHOOCH software [24]. The beam size at the sample was controlled by motorized slits to $0.1{-}0.2(\mathrm{h}) \times 0.1{-}0.2(\mathrm{v})\,\mathrm{mm}$, at typical primary beam flux densities of $I_0 = 7 \cdot 10^{12}\,\mathrm{cps/mm^2}$. The reflected beam was recorded in the vertical plane by a fast scintillation counter (Cyberstar, Oxford Danfysik), up to vertical momentum transfer of $q_z \simeq 0.8\,\text{Å}^{-1}$. To reduce unnecessary radiation dose during motor movement and in between scans, a fast shutter system was synchronized to the detector. Furthermore, the sample was translated horizontally to avoid damage, and attenuators were used for all measurement points at small q_z, counting statistics allowing. Reproducibility of the measured reflectivity and sample stability was controlled by measuring each curve at photon energies E_e, E_o, and back at E_e again, where $E_e = 13.475\,\mathrm{keV}$ denotes the Br K_α photon energy and $E_o = 13.228\,\mathrm{keV}$ an energy significantly far below the edge.

Analysis and results. – The quantitative data analysis was carried out in the framework of semi-kinematical reflectivity theory, which relates the decay of the reflectivity to the laterally averaged electron density profile $\rho_e(z)$ according to $\Phi(q_z) = |\frac{1}{\Delta\rho_{12}} \int \frac{\mathrm{d}\rho_e(z)}{\mathrm{d}z} \mathrm{e}^{\mathrm{i}q_z z}\mathrm{d}z|^2$, where $\Delta\rho_{12}$ is the net density contrast of the interface

[1] The calculation was performed with the chemical modelling software MOLECULAR MODELING PRO™.

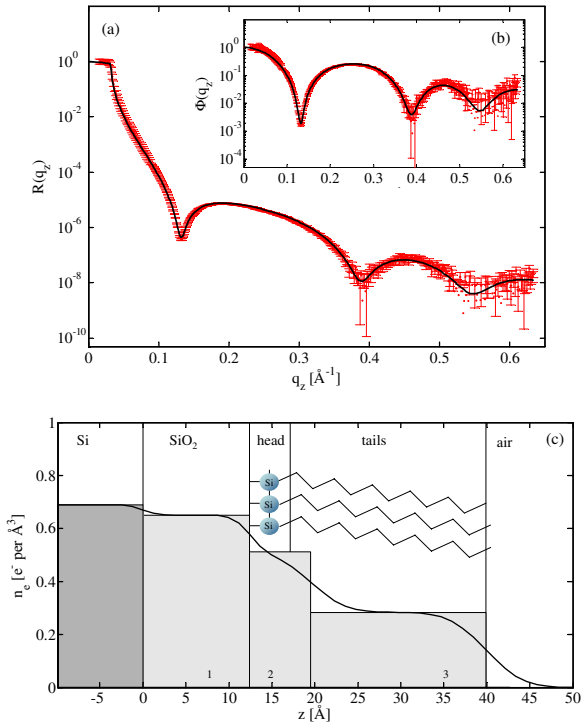

Fig. 2: (a) Normalized reflectivity curve $R(q_z)$ measured inhouse at an OTS sample in air along with the corresponding fit of a three-box model, which was used as a basis for the fitting of the more complicated OTS surfactant monolayers. (b) The same data and fit as in (a) is plotted here, but as $\Phi(q_z) = R(q_z)/R_F(q_z)$, *i.e.* divided by the Fresnel reflectivity. (c) Electron density profile corresponding to the fit in the upper graphs. The smooth profile is generated as a sum of Gaussian error functions, each illustrated by a box of certain density and width in the graph. Furthermore, the OTS molecules are depicted schematically, along with the subunit lengths from a *physical* interpretation of the profile. Note that the alkyl chains are tilted against the surface normal [25].

(*i.e.* silicon-water), and $\rho_e(z)$ is the laterally (xy-plane) averaged electron density profile [26].

In order to characterize the hydrophobic substrate material and to facilitate the analysis of measurements involving the more complicated supported monolayer systems, measurements of pure OTS samples were performed at a "D8 Advance" inhouse diffractometer (Bruker AXS, Germany) equipped with a sealed Mo tube, operating at the Mo-K_α energy $E = 17.478\,\mathrm{keV}$. The result of such a measurement is shown in fig. 2. The data has been fitted to a standard box bodel (cf. fit in fig. 2), describing the electron density profile of the OTS layer by three boxes, each parameterized by thickness, density and interfacial roughness [27,28]. In detail, one box was used to describe the native oxide layer on top of the silicon surface, one for the transition region with the OTS headgroup and one for the OTS tails. The oxide layer was modelled with thickness $d_{\mathrm{SiO_2}} = 12.4(\pm 0.5)$ Å and density $\rho_{\mathrm{SiO_2}} = 0.650(\pm 0.007)\,\mathrm{Å}^{-3}$ (see footnote [2]). It is noted that, in interpreting box model results, there is always some ambiguity in the representation of a given density profile by several combinations of boxes. More precisely, only the product of density and length of a box can be determined unambigiously in a fit, so that the length and height of a box cannot be identified directly with the physical dimension and density of a molecular subunit in complicated systems [29]. Following this argument, the shape of the modeled density curve provides the main orientaton for estimating physical properties of the sample, not the box dimensions alone. Thus, one can calculate the length of the OTS headgroup region as $d_{\mathrm{OTS}}^{(hd)} = 2/3 \cdot d_2 = 4.7(\pm 0.2)$Å and the length of the tail region as $d_{\mathrm{OTS}}^{(tl)} = 1/3 \cdot d_2 + 1 \cdot d_3 = 22.8(\pm 0.2)$Å. As there are only very small differences in the physical subunit lengths compared to the fitted box parameters, the box heights can directly be identified with the densities of the molecular subunits here ($\rho_{\mathrm{OTS}}^{(hd)} = \rho_2 = 0.512(\pm 0.005)\,\mathrm{Å}^{-3}$, $\rho_{\mathrm{OTS}}^{(tl)} = \rho_3 = 0.284(\pm 0.003)\,\mathrm{Å}^{-3}$). These results are in good aggreement with previous studies of silanized silicon surfaces [27,29] and indicate a homogeneous coverage of the OTS layer.

For the supported lipid monolayers, two to three additional boxes were used to describe the uppermost monolayer, one for the transition region between OTS and the surface layer, one for the surface layer tail region and, where appropriate, one for the headgroup. Importantly, in the fits of the mixed samples the DPPC headgroup density was reduced to an effective value $\rho_{\mathrm{eff}} = (1 - \alpha_{\mathrm{DAB}}) \cdot (\rho_{\mathrm{DPPC}} - \rho_{\mathrm{H_2O}}) + \rho_{\mathrm{H_2O}}$, accounting for the molar fraction $(1 - \alpha_{\mathrm{DAB}})$ of DPPC in the surface monolayer. The added counterion distribution has been modelled as a Poisson-Boltzmann distribution convoluted with a Gaussian of width ξ, accounting for interface roughness, thermal motion in the headgroup and finite experimental resolution, all leading to a smearing of the counterion profile given by

$$n(z) = \frac{\sigma_s}{\mu_{\mathrm{GC}}} \cdot \frac{1}{\sqrt{2\pi\xi^2}} \int_{-\infty}^{z} \frac{\exp\left(-\frac{\tau^2}{2\xi^2}\right)}{\left(1 + \frac{(z-\tau)}{\mu_{\mathrm{GC}}}\right)^2} \mathrm{d}\tau \,. \qquad (2)$$

The validity of this convolution approach was demonstrated in [16]. The counterion number distribution $n(z)$ is related to the counterion effective electron density $\Delta n_e(z)$ by $\Delta n_e(z) = Z_{\mathrm{eff}}(E) \cdot n(z)$. Here $Z_{\mathrm{eff}}(E) = f_{\mathrm{Br}}(E) - \nu_{\mathrm{Br}} \rho_e^{\mathrm{H_2O}}$ is the effective number of scattering bromide counterion electrons. The energy-dependent bromide scattering factor $f_{\mathrm{Br}}(E) \simeq f'_{\mathrm{Br}}(E) + f_{\mathrm{Br}}^{(0)}$ changes

[2] The experimental errors were estimated in the following way: The parameter p of interest was changed by a fraction π in comparison to its value obtained in the fit, while all other parameters were kept constant. The values π_{min} and π_{max}, at which the total reduced χ^2 of the original fit was increased by 25%, were determined. The average value $\pi = 0.5 \cdot (\pi_{\mathrm{min}} + \pi_{\mathrm{max}})$ was assumed to be the experimental error.

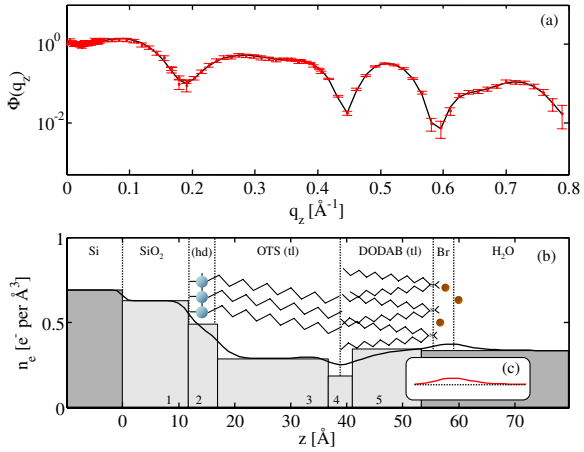

Fig. 3: (a) Normalized reflectivity curve of a pure DODAB monolayer on OTS, along with best slab model fit. (b) Density profile corresponding to the fit shown in (a). The boxes of the slab model are illustrated along with the physical interpretation of the resulting density profile. The counterion cloud is modelled separately with a Poisson-Boltzmann approach as described in the text. (c) Counterion component of the density profile, according to a convoluted Poisson-Boltzmann model (cf. main text)).

by ca. 10–15% between the energies E_e and E_o and is reduced by the number of bulk (water) electrons $\nu_{\mathrm{Br}}\rho_e^{\mathrm{H_2O}}$ contained in one bromide ionic volume ν_{Br}, given a water electron density of $\rho_e^{\mathrm{H_2O}} = 0.334\,\text{Å}^{-3}$. A free reference position z_0 of the counterion distribution $n(z) = n'(z - z_0)$ was allowed in the fit. Thus, the distribution is determined by three fit parameters, the Gouy-Chapman length $\mu_{\mathrm{GC}} = (2\pi\ell_B\sigma_s)^{-1}$, the Gaussian width ξ and the reference position z_0.

In fig. 3 a sketch of the fitted slab model density profile for $\alpha_{\mathrm{DAB}} = 1$ is shown. The fit was performed based on the results of the previous fits for the OTS layer in air. However, the parameters describing the OTS layer were not fixed in the new fits, as freshly prepared samples were used at the synchrorton experiments, following the same preparation pathway as for the in-house experiments. Small changes in the fit parameters were observed, still consistent with previous results published on OTS [27,29]. The density profile is also illustrated in fig. 3. Obviously, the global minimum of the profile, at $z_{\min} = 38.8(\pm 0.1)\,\text{Å}$, marks the center of the OTS/DODAB transition region. Keeping the length of $d_{\mathrm{OTS}}^{(hd)}$ as shown in fig. 2, one obtaines $d_{\mathrm{OTS}}^{(tl)} = z_{\min} - d_{\mathrm{SiO_2}} - d_{\mathrm{OTS}}^{(hd)} = 22.3(\pm 0.4)\,\text{Å}$, which is almost the same length of the OTS tail region as measured for pure OTS (22.8 Å). The difference can be regarded as a measure for the experimental uncertainty of $d_{\mathrm{OTS}}^{(tl)}$, as it is not expected that the chain length or tilt angle changes considerably from the pure monolayer to the coated monolayer. Consequently, the position of the minimum is very consistent with the measurement of OTS in air.

The length of the DODAB molecules can be estimated as $d_{\mathrm{DAB}}^{(tl)} = 0.5 \cdot d_4 + d_5 + d_{\mathrm{CI}} - 0.5 \cdot a$, where $a = 3.7\,\text{Å}$ is the bromide ionic diameter [12]. One obtaines $d_{\mathrm{DAB}}^{(tl)} = 16.6(\pm 0.4)\,\text{Å}$, which is consistent with half the thickness of DODAB bilayers [30]. As explained before, the DODAB headgroup is practically invisible to the X-ray probe. Therefore, the last maximum in the profile can be regarded to be caused solely by the bromide counterions. The counterion cloud is illustrated in fig. 3 as a further layer of approximate thickness $a = 3.7\,\text{Å}$. As visible in fig. 3, the position of this "layer" marks the center of the counterion cloud in the immediate vicinity of the headgroup, indicating that the given physical interpretation of the fitted profile is well suited to describe the experimental system.

The fitted parameters for the counterion cloud as shown in fig. 3 were given by a surface ion number density $\sigma_s = 0.018(\pm 0.04)\,\text{Å}^{-2}$, peak width $\xi = 2.7(\pm 0.2)\,\text{Å}$ and reference position $z_0 = 57.4(\pm 0.6)\,\text{Å}$. Correspondingly, an area per charge of $A_c = \sigma_s^{-1} = 55(\pm 5)\,\text{Å}^2$ was obtained, indicating very precisely a 1 : 1 ratio of counterions to DODAB molecules, as expected in the salt-free case[3]. The resonance effect was determined to be very small, on the border of the detection level, when all uncertainties due to sample preparation, drift, instrumental stability, counting statistics and fitting reproducibility are quantified. However, for the case of pure DODAB, the sample with the highest density of resonantly scattering bromide atoms, a small difference could be observed between measurements at photon energies equal to the bromide K_α energy $E_e = 13.475\,\text{keV}$, and away from the absorption edge, at $E_o = 13.228\,\text{keV}$. The two measurements are depicted in fig. 4(a). As visible from the figure, the measurement with higher bromide scattering power ($E = 13.228\,\text{keV}$) shows a small local minimum at $q \cdot \text{Å} \in [0.25, 0.4]$, not visible in the other measurement. The explanation of the small, but yet detectable resonance effect for $\alpha_{\mathrm{DAB}} = 1.0$, along with the fact that more localized counterion distributions (*i.e.* $\xi < 2\,\text{Å}$) could be ruled out by simulations (not shown here), is a strong indication for the validity of the chosen model.

Representative reflectivity curves $\Phi(q_z) = R(q_z)/R_{\mathrm{F}}(q_z)$ for the charge dilution series ($\alpha_{\mathrm{DAB}} = 1,\ 0.5,\ 0.25,\ 0$) are shown in fig. 5, normalized by the Fresnel reflectivity $R_{\mathrm{F}}(q_z)$ to highlight the q_z-modulation of the reflectivity curve. A characteristic and reproducible feature in the DPPC reflectivity curve is a pronounced minimum at $\simeq 0.3\,\text{Å}^{-1}$. This minimum disappears gradually, when the neutral DPPC is replaced by the charged DODAB in the surface monolayer.

In contrast to the case of pure DODAB ($\alpha_{\mathrm{DAB}} = 1.0$), no systematic differences in the data obtained at different photon energies could be observed for $\alpha_{\mathrm{DAB}} = 0.5,\ 0.25$, due to the strongly reduced resonance contrast. However,

[3]The area per headgroup, $A - h$, for a DODAB monolayer is known to be $A - h \approx 50\,\text{Å}^2$ [22,23].

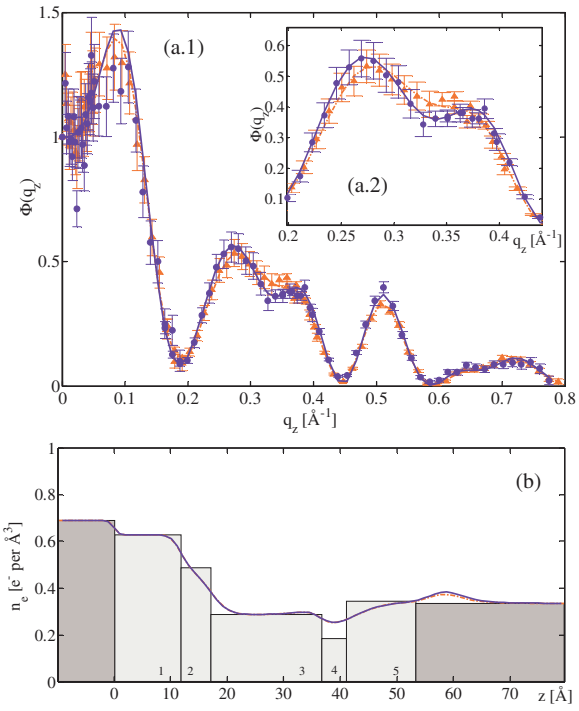

Fig. 4: (a.1 and magnification in inset a.2) Reflectivity measurements of pure DODAB on OTS, normalized by Fresnel reflectivity. Between both measurements the photon energy was changed from the bromide K_α energy $E = 13.475\,\mathrm{keV}$ (red, dash-dotted line) to 13.228 keV (blue, solid line). Along with the measurements, corresponding fits are shown. (b) Density profiles corresponding to fits shown in (a). While for $E = 13.475\,\mathrm{keV}$ all parameters were fitted, for $E = 13.228\,\mathrm{keV}$ only the energy was changed in the underying formulae to the new value. All other parameters were kept equal.

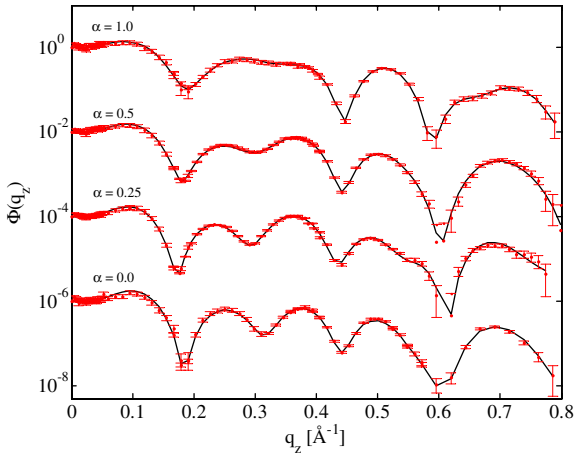

Fig. 5: Normalized reflectivity curves for different molar fractions α_{DAB} of DODAB in the DODAB/DPPC mixtures, shifted vertically for clarity. The solid lines indicate the best fits derived from a modified slab model, incorporating a counterion contribution and the reduced DPPC headgroup density according to its respective molar fraction $(1 - \alpha_{\mathrm{DAB}})$.

the data presented in fig. 5 could be consistently modelled in the fits by a gradual decrease of the surface charge density σ_s, proportional to the decrease in the DODAB

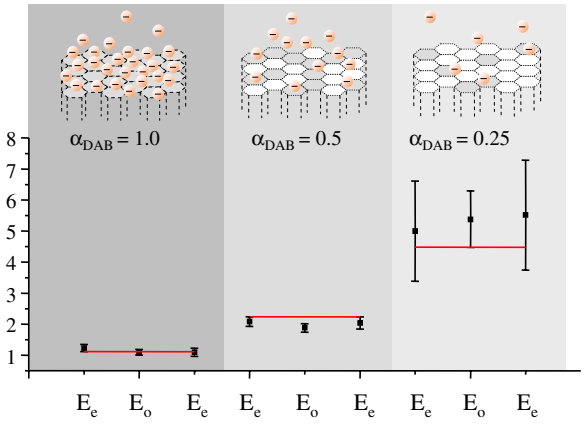

Fig. 6: Gouy-Chapman lengths resulting from fits to reflectivities of samples with different molar fractions α_{DAB} of DODAB. The values are given for three consecutive measurements, carried out firstly at energy E_e, secondly at E_o and lastly —to check reproducibility— back at E_e again. The solid red curves represent theoretical values for $A_c = A_c^{(0)} = 50\,\mathrm{Å}^2$ in the case $\alpha_{\mathrm{DAB}} = 1$, $A_c = 0.5 \cdot A_c^{(0)}$ for $\alpha_{\mathrm{DAB}} = 0.5$ and $A_c = 0.25 \cdot A_c^{(0)}$ for $\alpha_{\mathrm{DAB}} = 0.25$ according to the well-known area per headgroup for a DODAB monolayer, $A_h \approx 50\,\mathrm{Å}^2$ [22,23].

molar fraction α_{DAB}. This decrease in the charge density corresponds to an inversely proportional increase in the area per charge and the Gouy-Chapman-length μ_{GC}, as described before. The resulting values of μ_{GC} are depicted in fig. 6: As expected, μ_{GC} increases proportionally to the inverse charged molar fraction $1/\alpha_{\mathrm{DAB}}$ in the sample, indicating again quite well a 1 : 1 ratio of bromide ions and DODAB molecules in the sample. A representative value for the fitted widths of the counterion cloud is $\xi = 2.6(\pm 0.7)\,\mathrm{Å}$.

In a second, independent analysis approach, which can be regarded as a limit case of the box model for a very large number of boxes, an unbiased model for the laterally averaged electron density $\rho_e(z)$ was applied [31] to yield a counterion distribution, practically independent of subjective modelling assumptions. Here $\rho_e(z)$ was modelled as a sum of step functions, convoluted with a Gaussian profile of standard deviation ϵ, linked to the experimental resolution $d_r = \pi/q_{\max} \approx 4\,\mathrm{Å}$ via $\mathrm{FWHM}(\epsilon) = 2\sqrt{2\ln 2} \cdot \epsilon = d_r$. The normalized convoluted profile is given by $\frac{\rho_e(z)}{\Delta\rho} = 1 + \frac{1}{2}\sum_{j=0}^{N}\left(a_j \cdot \mathrm{erfc}\left(\frac{j\mathrm{d}z - z}{\sqrt{2\epsilon^2}}\right)\right)$ with N parameters a_j and a real space step width dz. Typically, $N \approx 100$ and $dz = 0.25 \cdot d_r$ were used. The parameter refinement was carried out applying the differential evolution algorithm [32]. In addition to the normalization $(\sum_{j=0}^{N} a_j = -1)$ and boundary conditions $(a_0 = 0,\ a_N = 0)$ the possible a_j were restricted by the choice of a suitable start ensemble comprising possible profiles. It is a well-known effect of this method that a statistical ensemble of runs yields separate classes of systematically different results reflecting the infinite amount of possible profile reconstructions. The physically unreasonable classes

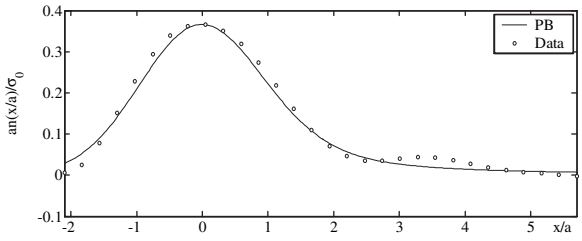

Fig. 7: Counterion number distribution extracted from a free-form fit (open circles) for a DODAB sample from a measurement at $E_e = 13.475\,\mathrm{keV}$, rescaled in dimensionless units based on the Br ion diameter a. In addition, the best simulation for a convoluted PB distribution is shown (solid line), with $\xi = 3.25\,\mathrm{\AA}$.

can be ruled out, leaving one group of profiles that is averaged to yield the most probable result [31]. From the total electron density profiles $\rho_e(z)$ the corresponding counterion density distributions were obtained for $\alpha_{\mathrm{DAB}} = 1$ by subtracting a straight line, accounting for the water background. A representative distribution is shown in fig. 7. The resulting profile could be modelled quite well with a convoluted Poisson-Boltzmann distribution (cf. also fig. 7), yielding very similar widths $\xi = 3.0(\pm 0.4)\,\mathrm{\AA}$ and Gouy-Chapman lengths $\mu_{\mathrm{GC}} = 1.0 \times (\pm 0.2)\,\mathrm{\AA}$ as obtained from the box model analysis for $\alpha_{\mathrm{DAB}} = 1$. The occurrence of a minor second maximum in the distribution is systematic, but the experimental resolution d_r is too low to allocate the second maximum with high certainty to a second diffuse counterion layer.

Summary and conclusions. – In summary, we have shown by synchrotron-based X-ray reflectivity that the counterion distribution near a charged wall under salt-free conditions is in good agreement with a convoluted Poisson-Boltzmann distribution, within the experimental accuracy. In quantitative agreement with the PB model, the degree of diffusiveness in the ion cloud varies with the surface charge. The results, obtained by a standard box model with an added counterion contribution and a model-independent analysis method, agree well with a previous study applying Debye-Hueckel theory for non-vanishing bulk electrolyte solutions [10,11]. However, in contrast to previous results on acidic systems, no renormalization of the surface charge by competitive binding of hydronium was necessary in the modelling. Furthermore, the results show that no bound Stern layer or partial counterion condensation was observed, at least not to the degree, which is distinguishable after convolution with a Gaussian of widths $\xi = 3.0\,\mathrm{\AA}$, taking into account finite ion size and interfacial roughness. In fact, it is the roughness of the charged surface as much as the experimental resolution, which limits the quantitave verification of the PB model.

* * *

It is a pleasure to thank P. Boesecke and H. Metzger for providing excellent working conditions at the ID01 beamline, ESRF for beamtime, E. Novakova for help and discussion, A. Beerlink for support during the beamtime, and K. Jacobs for providing silanized silicon wafers. Funding through the French German network "Complex fluids" (grant SA 772/7-1) by DFG is gratefully acknowledged.

REFERENCES

[1] Gouy G., *J. Phys. (Paris)*, **9** (1910) 455.
[2] Chapman D. L., *Philos. Mag.*, **25** (1913) 475.
[3] Debye P. and Hückel E., *Phys. Z.*, **24** (1923) 185.
[4] Netz R. R., *J. Phys: Condens. Matter*, **16** (2004) 2353.
[5] Das R. *et al.*, *Phys. Rev. Lett.*, **90** (2003) 188103.
[6] Andresen K. *et al.*, *Phys. Rev. Lett.*, **93** (2004) 248103.
[7] Guilleaume B. *et al.*, *Eur. Phys. J. E*, **8** (2002) 299.
[8] Richardsen H. *et al.*, *Europhys. Lett.*, **34** (1996) 543.
[9] Kirchner S., *Biochim. Biophys. Acta*, **1279** (1995) 181.
[10] Bu W. *et al.*, *Phys. Rev. E*, **72** (2005) 060501.
[11] Bu W. *et al.*, *Langmuir*, **22** (2006) 5673.
[12] Luo G. *et al.*, *Science*, **311** (2006) 216.
[13] Park C. *et al.*, *Phys. Rev. Lett.*, **97** (2006) 016101.
[14] Moreira A. G. and Netz R. R., *Eur. Phys. J. E*, **8** (2002) 33.
[15] Netz R. R., *Phys. Rev. Lett.*, **91** (2003) 138101.
[16] Fleck C. C. and Netz R. R., *Phys. Rev. Lett.*, **95** (2005) 128101.
[17] Sagiv J., *J. Am. Chem. Soc.*, **92** (1980) 102.
[18] Kalb E. *et al.*, *Biochim. Biophys. Acta*, **1103** (1992) 307.
[19] Richter R. P. *et al.*, *Langmuir*, **22** (2006) 3497.
[20] Linseisen F. M. *et al.*, *Chem. Phys. Lipids*, **83** (1996) 9.
[21] Vogel M. *et al.*, *Phys. Rev. Lett.*, **84** (2000) 390.
[22] Moura S. P. and Charmona-Ribeiro A., *Langmuir*, **19** (2003) 6664.
[23] Shapovalov V. and Tronin A., *Langmuir*, **13** (1997) 4870.
[24] Evans G. and Pettifer R., *J. Appl. Crystallogr.*, **34** (2001) 92.
[25] Schreiber F., *Prog. Surf. Sci.*, **65** (2000) 151.
[26] Als-Nielsen J. and Mcmorrow D., *Elements of Modern X-Ray Physics* (John Wiley & Sons, Chichester, UK) 2001.
[27] Tidswell I. M. *et al.*, *Phys. Rev. B*, **41** (1990) 1111.
[28] Strzalka J. *et al.*, *Phys. Rev. E*, **70** (2004) 051603.
[29] Mezger M. *et al.*, *Proc. Natl. Acad. Sci. U.S.A.*, **103** (2006) 18401.
[30] Pereira E. M. A., Petri D. F. S. and Carmona-Ribeiro A. M., *J. Phys. Chem. B*, **110** (2006) 10070.
[31] Politsch E. and Cevc G., *J. Appl. Crystallogr.*, **35** (2002) 347.
[32] Storn R. and Price K., *J. Glob. Optim.*, **11** (1997) 341.